Rock Mech Rock Eng (2015) 48:1605–1622
DOI 10.1007/s00603-014-0652-3

ORIGINAL PAPER

# Rate-Dependent Embedded Discontinuity Approach Incorporating Heterogeneity for Numerical Modeling of Rock Fracture

**Timo Saksala**

Received: 16 April 2014 / Accepted: 12 September 2014 / Published online: 19 September 2014


**Abstract** In this paper, the embedded discontinuity approach is applied in finite element modeling of rock in compression and tension. For this end, a rate-dependent constitutive model based on (strong) embedded displacement discontinuity model is developed to describe the mode I, mode II and mixed mode fracture of rock. The constitutive model describes the bulk material as linear elastic until reaching the elastic limit. Beyond the elastic limit, the rate-dependent exponential softening law governs the evolution of the displacement jump. Rock heterogeneity is incorporated in the present approach by random description of the mineral texture of rock. Moreover, initial microcrack population always present in natural rocks is accounted for as randomly-oriented embedded discontinuities. In the numerical examples, the model properties are extensively studied in uniaxial compression. The effect of loading rate and confining pressure is also tested in the 2D (plane strain) numerical simulations. These simulations demonstrate that the model captures the salient features of rock in confined compression and uniaxial tension. The developed method has the computational efficiency of continuum plasticity models. However, it also has the advantage, over these models, of accounting for the orientation of introduced microcracks. This feature is crucial with respect to the fracture behavior of rock in compression as shown in this paper.

T. Saksala (✉)
Department of Mechanical Engineering and Industrial Systems, Tampere University of Technology, P.O.Box 589, 33101 Tampere, Finland
e-mail: timo.saksala@tut.fi

**Keywords** Uniaxial compression · Rock fracture · Embedded discontinuities · Confined compression · Finite elements

## 1 Introduction

Numerical modeling of rock fracture has become an active area of research in the field of computational mechanics due to its importance in failure analyses of underground rock structures and rock breakage industry. The major challenges in this field are, generally, related to numerical modeling of crack propagation and, particularly, to description of rock microstructure. The two primary factors affecting the mechanical behavior of rock are its heterogeneity, due to different minerals with different material properties and various grain sizes and shapes, and inherent microdefects, such as microcracks, pores and inclusions (Jaeger and Cook 1971; Mahabadi 2012; Liu et al. 2004a; Tang 1997; Xia et al. 2008; Wei and Anand 2008; Krajcinovic 1996; Tang and Hudson 2010). Therefore, it is beneficial if both of these factors are taken into account in numerical modeling aiming at realistic description of rock fracture.

In addition to these microstructural factors, the external loading and its rate also affect the microscopic processes of fracture and, consequently, the corresponding macroscopic failure mode. The effect of confinement or lateral pressure in compression of cylindrical rock specimen is roughly as follows (Wei and Anand 2008; Krajcinovic 1996): (1) In the low-confinement regime, grain-boundary sliding and inherent microcrack population-induced crack initiation, growth and coalescence will result in large inelastic deformation, macroscopic dilatancy and brittle faulting with axial splitting failure mode with single or multiple

axial macrocracks (Paterson 1958; Jia et al. 2013). It is observed many times, also in uniaxial compression, that the axially-oriented microfaults (e.g. mode I microcracks) link together to form a slanted macrofault (shear band) (Szwedzicki 2007). (2) At intermediate confining pressure, grain boundary microcracking becomes more distributed and, during strain-softening stage, localizes to form macroscopic shear bands. (3) On still increasing confinement, the grain boundary sliding is suppressed by friction leading to disappearance of dilatancy effects and onset of grain interior plasticity to accommodate the restricted external deformation. This brittle-to-ductile transition is exhibited at room temperatures and pressures accessible in the laboratory by compact carbonate rocks (e.g. marble and limestone). With these rocks, the shear stresses required to grain interior plasticity activation is relatively low (Wei and Anand 2008).

The influence of rock microstructure on the deformation and failure processes in uniaxial compression was studied by Pininska (2008) on the basis of experiments on several hundreds of Polish rocks. It was found that the main destabilizing factor for rocks with regular-grained and compact structure bonded with strong cement is the brittle intragranular fracture of single grains. Consequently, extensive microcracks appear inside grains without dilatancy. The related failure mechanism is a burst-like loss of stability of the rock structure resulting in multiple fragmentation of the sample. In carbonate rocks with grains randomly distributed in a weak matrix and rocks containing soft irregularly shaped grains, intergranular microcracks leading to failure of the sample initiate by structural (micro) defects. In the related post-critical stage of the failure process, macrocracking is shear fracture-dominated. These findings are relevant in the present numerical study. The effect of loading rate is that increased loading rate increases the peak stress and leads to multiple fragmentation of rock samples (Zhang and Zhao 2014).

Many numerical approaches have been developed during the last two and half decades for simulating the rock fracture in uniaxial and confined compression. Tang (1997) introduced his rock failure process analysis (RFPA) code where the rock fracture is modeled with a simple isotropic damage model and rock heterogeneity is described at the mesoscopic level using the Weibull distribution. Liu et al. (2004a) modified the code (resulting in R-T$^{2D}$ code) with a double-elliptic fracture criterion. Saksala developed (2010) a damage-viscoplastic consistency model with parabolic cap for rocks with brittle and ductile behavior under low-velocity impact loading. Fang and Harrison (2002a) developed a local degradation model for brittle fracture in heterogeneous rocks. They applied the model, as implemented in the fast Lagrangian analysis of continua (FLAC) code, for modeling confined compression Fang and Harrison (2002b). In the model for geomaterials under tension and compression, by Klerck et al. (2004), a discrete crack is introduced (and followed by remeshing) in the mesh when a tensile strength is exhausted in the principal direction. Combined finite element method/discrete element method (FEM/DEM) approach by Mahabadi et al. (2010) and (2012) seems very promising for fragmentation analyses. The model describes the microstructure of rock through the image analysis and mineral mapping method. In the numerical study on brittle-to-ductile transition by Wei and Anand (2008), the rock microstructure is represented as Voronoi-tessellated grains. The grain-interior failure is accounted for by standard plasticity model while the grain-boundary cracking is modeled by a cohesive law for shear and tension. Sellers and Napier (1997) developed a boundary element code for modeling fracture formation in deep gold mine excavations. Particle-based models are applied also by Yoon et al. (2012), Ma et al. (2011) and Jia et al. (2013). Finally, the cellular automata-based 3D numerical study by Pan et al. (2009) is recognized.

In the present work, the embedded discontinuity approach is applied in numerical modeling of rock under tension and compression. For this end, a rate-dependent embedded displacement discontinuity model with constant displacement jumps both in normal and tangential directions is developed to describe the mode I, mode II and mixed mode fracture of rock. The rate dependency is incorporated via viscosity. The works by Simo et al. (1993), Simo and Oliver (1994) and Oliver (1996a, b) are referred here to as the early developments of the method. This approach is particularly suitable for the description of inherent microcrack populations present in natural rocks. The microstructure of rock is incorporated into the model by random description of the mineral texture of rock. This model is applied in 2D simulation confined compression test. The model properties are extensively studied in uniaxial compression. The effect of confinement and loading rate are tested as well.

## 2 Theory of the Model

The theory of the model for rock fracture based on the embedded strong discontinuity approach is presented in this section. Moreover, the methods for heterogeneity and initial crack population description are briefly explained.

### 2.1 Strong Discontinuity Kinematics

Consider a body occupying domain $\Omega$ in $\mathbf{R}^2$ with a boundary $\partial\Omega$ (see Fig. 1). The body is split into two disjoint parts $\Omega^+$ and $\Omega^-$ by a strong discontinuity line $\Gamma_d$ (crack) defined by its normal $\mathbf{n}$ and tangent $\mathbf{m}$. Then the

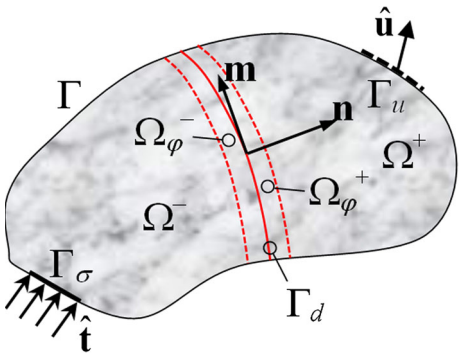


**Fig. 1** Domain crossed by a discontinuity line

displacement field of a particle in the body can be decomposed as a function of the location $\mathbf{x} \in \Omega$ as

$$\mathbf{u}(\mathbf{x}) = \bar{\mathbf{u}}(\mathbf{x}) + \underbrace{(H_{\Gamma_d}(\mathbf{x}) - \phi(\mathbf{x}))}_{M_{\Gamma_d}(\mathbf{x})} \mathbf{u}(\mathbf{x}) \tag{1}$$

where $\bar{\mathbf{u}}(\mathbf{x})$ stands for the regular displacement field, $\mathbf{u}(\mathbf{x})$ is the displacement jump at $\Gamma_d$ due to discontinuity, and $H_{\Gamma_d}(\mathbf{x})$ is the Heaviside function at the discontinuity. Function $\phi(\mathbf{x})$ is defined in an arbitrary subdomain $\Omega_\phi = \Omega_\phi^+ \cup \Omega_\phi^-$ so that $\phi(\mathbf{x}) = 0$ when $\mathbf{x} \in \Omega^- \backslash \Omega_\phi^-$, $\phi(\mathbf{x}) = 1$ when $\mathbf{x} \in \Omega^+ \backslash \Omega_\phi^+$, and it is $C^0$-continous between 0 and 1 when $\mathbf{x} \in \Omega_\phi$. Decomposition (1) is used, instead the natural one with $\phi(\mathbf{x}) \equiv 0$, since it facilitates an easier treatment of the essential boundary conditions in the finite element (FE) context. More specifically, as both $\bar{\mathbf{u}}$ and $\mathbf{u}$ may be nonzero at boundary $\partial\Omega$, it is more convenient to use decomposition (1) since $\varphi$ restricts the effect of the displacement jump to subdomain $\Omega_\phi$.

Infinitesimal deformation kinematics assumption leads to the following strain field (Feist and Hofstetter 2006)

$$\boldsymbol{\varepsilon}(\mathbf{x}) = \underbrace{\nabla^s \bar{\mathbf{u}}(\mathbf{x}) - (\mathbf{u} \otimes \nabla\phi(\mathbf{x}))^{sym}}_{\bar{\varepsilon}} + \underbrace{\delta_{\Gamma_d}(\mathbf{x})(\mathbf{u} \otimes \mathbf{n})^{sym}}_{\boldsymbol{\varepsilon}_\delta} \tag{2}$$

where the result $\nabla H_{\Gamma_d} = \delta_{\Gamma_d}\mathbf{n}$ on Dirac delta function $\delta_\Gamma$ is used. Moreover, constant displacement jump is assumed yielding $\nabla^s \mathbf{u} = \mathbf{0}$. The first two terms on the right hand side of (2) defined in the bulk, i.e. in $\Omega \backslash \Gamma_d$, comprise the regular strain $\bar{\varepsilon}(\mathbf{x})$ while the third term is singular strain $\boldsymbol{\varepsilon}_{\delta_d}(\mathbf{x})$ defined in the discontinuity.

### 2.2 Finite Element Implementation of Strong Discontinuity Kinematics

Consider the body described in Fig. 1 being discretized with the constant strain triangle (CST) elements. With this choice the embedded discontinuity is a straight line. The finite element implementation is illustrated in Fig. 2.

The finite element discretized version of Eqs. (1) and (2) are

$$\begin{aligned} \mathbf{u}(\mathbf{x}) &= N_i \mathbf{u}_i^e + \underbrace{\left(H_{\Gamma_d}(\mathbf{x}) - N^{sol}(\mathbf{x})\right)}_{M^e_{\Gamma_d}} \boldsymbol{\alpha}_d \\ \boldsymbol{\varepsilon}(\mathbf{x}) &= (\nabla N_i \otimes \mathbf{u}_i^e)^{sym} - (\nabla N^{sol}(\mathbf{x}) \otimes \boldsymbol{\alpha}_d)^{sym} + \delta_{\Gamma_d}(\mathbf{n} \otimes \boldsymbol{\alpha}_d)^{sym} \end{aligned} \tag{3}$$

where $\boldsymbol{\alpha}_d$ denotes the displacement jump and $N_i$ and $\mathbf{u}_i^e$ are the standard (linear with CST) interpolation functions and nodal displacements ($i = 1,2,3$ with summation on repeated indices), respectively. Thus, in the finite element context function $\varphi$ in Eq. (1) is identified with the interpolation function $N^{\text{sol}}$ related to the solitary node, $s^{\text{sol}}$, with a single element support.

Applying the standard arguments to the discrete form of the balance of linear momentum, the following symmetric, kinematically consistent FE formulation can be derived (Huespe et al. 2006; Huespe and Oliver 2011):

$$\begin{aligned} &\int_{\Omega_e} \rho N_i N_j \ddot{\mathbf{u}}_j \, d\Omega + \int_{\Omega_e} \boldsymbol{\sigma} \cdot \nabla N_i d\Omega - \int_{\Gamma_\sigma} N_i \hat{\mathbf{t}} d\Gamma = \mathbf{0}, \\ &\quad i,j = 1 \ldots N_{nodes} \\ &- \int_{\Omega_e} \boldsymbol{\sigma} \cdot \nabla N^{sol} d\Omega^e + \int_{\Gamma_d} \mathbf{t}_{\Gamma_d} \, d\Gamma_d = \mathbf{0}, \quad \forall e \in J \end{aligned} \tag{4}$$

where $N_{nodes}$ is the number of nodes in the mesh, $J$ denotes the set of elements with an embedded discontinuity, and $N_i$ is the interpolation function of node $i$. The second equation which imposes a weak equilibrium across the discontinuity $\Gamma_d$, can be further simplified in case of CST element with constant displacement jump (yielding constant traction). This simplification, is written here with the local (strong) form of equilibrium as

$$\begin{aligned} \mathbf{t}_{\Gamma_d} &= \frac{\Omega_e}{l_d} \boldsymbol{\sigma} \cdot \nabla N^{sol} \\ \mathbf{t}_{\Gamma_d} &= \boldsymbol{\sigma} \cdot \mathbf{n} \end{aligned} \tag{5}$$

where $l_d$ is the length of the discontinuity. Therefore, this kinematically-consistent variational formulation requires that the length (area in 3D) of the discontinuity must be known a priori (Sancho et al. 2007). Tracking algorithms are usually employed for determining the length and position of the discontinuity. Inconveniently, this requires an extra problem, such as steady-state heat conduction, to be solved (Huespe and Oliver 2011).

There exists, however, another non-symmetric FE formulation, originally presented by Simo et al. (1993), Simo and Oliver (1994), based on the enhanced assumed strains (EAS) where the enhanced modes are constructed in the strain space, orthogonal to the stress field. There is still a third approach chosen in this paper which is a hybrid exploiting the advantages of both formulations, i.e. the

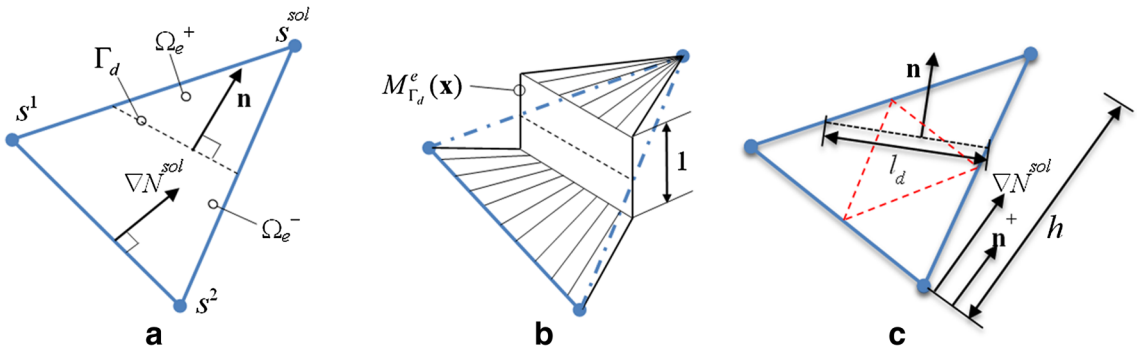


**Fig. 2** CST element with a discontinuity line (**a**), function $M_{\Gamma_d}$ (**b**) and geometrical definitions (**c**)

kinematic field is enhanced according to Eq. (3), while the EAS approach is used in calculating the internal forces and imposing the traction continuity. This formulation is obtained by replacing $(4)_2$ with the following average values:

$$\frac{1}{\Omega_e}\int_{\Omega_e\setminus\Gamma_d}\boldsymbol{\sigma}\cdot\mathbf{n}d\Omega=\frac{1}{l_d}\int_{\Gamma_d}\overbrace{\boldsymbol{\sigma}_{\Gamma_d}\cdot\mathbf{n}}^{\mathbf{t}_{\Gamma_d}}d\Gamma_d=\mathbf{0} \tag{6}$$

The integrands in (6) are constants for the CST element (and linear tetrahedron in 3D) and, thus, (6) becomes the local (exact) equilibrium condition $(5)_2$ for the tractions across the discontinuity. It should be emphasized that the EAS concept-based formulation provides a very simple implementation as neither the explicit position of the discontinuity line within the element nor the length of it are necessary to be known. Only the relative position of the discontinuity with respect to the element nodes is required for the calculation of function $N^{sol}$ related to the solitary node (Sancho et al. 2007). For these reasons, the EAS-based approach is chosen here for the following developments.

The selection of the solitary node $s^{sol}$ is based on the idea of Sancho et al. (2007). Thereby, the solitary node is chosen so that $\mathbf{n}$ and $\nabla N^{sol}$ are as parallel as possible. This is achieved by following criterion:

$$\nabla N^{sol}=\arg\left(\max_{i=1,2,3}\frac{|\nabla N_i\cdot\mathbf{n}|}{||\nabla N_i||}\right) \tag{7}$$

It is worth mentioning that all three forms are equal with CST elements (and linear tetrahedra in 3D) if the displacement discontinuity line is parallel to one of the sides of the triangle and the discontinuity line is located at the mid height of the element (see Fig. 2c) (Sancho et al. 2007). In this case

$$\mathbf{n}=\frac{\nabla N^{sol}}{||\nabla N^{sol}||}=\frac{\mathbf{n}^+}{h} \tag{8}$$

and $l_d h=\Omega_e$ with the terminology in Fig. 2c being used. This reorientation of the crack normal is tested in the numerical simulations in addition to the usual assumption that the crack is perpendicular to the major principal direction $\mathbf{n}$.

### 2.3 Rate-Dependent Discontinuity Model and Determination of the Displacement Jump

A bi-surface discontinuity model accounting for mode I and II fracture modes is sketched here for solving the displacement jump. Due to the formal similarity between the embedded discontinuity theory and classical plasticity, the present model can be cast in the form of the visco-plastic consistency model by Wang et al. (1997). The model employs following loading functions:

$$\begin{aligned}\varphi_{\mathrm{t}}(\mathbf{t}_{\Gamma_d},\kappa,\dot{\kappa})&=\underbrace{\mathbf{n}\cdot\mathbf{t}_{\Gamma_d}}_{\boldsymbol{\sigma}:(\mathbf{n}\otimes\mathbf{n})}-(\sigma_{\mathrm{t}}+q(\kappa,\dot{\kappa}))\\ \varphi_{\mathrm{s}}(\mathbf{t}_{\Gamma_d},\kappa,\dot{\kappa})&=\underbrace{|\mathbf{m}\cdot\mathbf{t}_{\Gamma_d}|}_{|\boldsymbol{\sigma}:(\mathbf{m}\otimes\mathbf{n})|}-(\sigma_{\mathrm{s}}+\tfrac{\sigma_{\mathrm{s}}}{\sigma_{\mathrm{t}}}q(\kappa,\dot{\kappa}))\end{aligned} \tag{9}$$

where $\mathbf{n}$ and $\mathbf{m}$ are the unit normal and tangent vectors for the crack surface, $\boldsymbol{\sigma}$ is the bulk stress while $\sigma_{\mathrm{t}}$ and $\sigma_{\mathrm{s}}$ denote the elastic limits in tension and shear, respectively. Furthermore, $\kappa,\dot{\kappa}$ are the internal variable and its rate is related to the softening law for discontinuity. Fixed crack concept is adopted here, i.e. $\mathbf{n}$ remains the same after introducing a discontinuity in an element. Therefore, it is necessary to allow for relative tangential sliding to prevent locking by unlimited shear stress generation in non-proportional loading states.

Following exponential softening law is assumed for softening variable $q$:

$$\begin{aligned}q&=h\kappa+s\dot{\kappa}\\ h&=-\frac{\sigma_{\mathrm{t}}^2}{G_{\mathrm{Ic}}}\exp(-\tfrac{\sigma_{\mathrm{t}}}{G_{\mathrm{Ic}}}\kappa)\end{aligned} \tag{10}$$

where $G_{\mathrm{Ic}}$ is the mode I fracture energy and $s$ is the constant viscosity modulus. This model couples the two fracture modes consistently, since the corresponding elasticity limits are chosen so that the full stress reduction is achieved simultaneously.

Evolution laws, similar to those in classical plasticity, are written for the displacement jump at the discontinuity and the internal variable as (Brancherie and Ibrahimbegovic 2009)

$$\dot{\boldsymbol{\alpha}}_{\mathrm{d}} = \dot{\boldsymbol{\alpha}}_{\mathrm{I}} + \dot{\boldsymbol{\alpha}}_{\mathrm{II}} = \dot{\lambda}_{\mathrm{t}} \frac{\partial \varphi_{\mathrm{t}}}{\partial \mathbf{t}_{\Gamma_d}} + \dot{\lambda}_{\mathrm{s}} \frac{\partial \varphi_{\mathrm{s}}}{\partial \mathbf{t}_{\Gamma_d}} = \dot{\lambda}_{\mathrm{t}} \mathbf{n} + \dot{\lambda}_{\mathrm{s}} \mathbf{m} \cdot \mathrm{sgn}(\mathbf{t}_{\Gamma_d} \cdot \mathbf{m})$$
$$\dot{\kappa} = \dot{\lambda}_{\mathrm{t}} \frac{\partial \varphi_{\mathrm{t}}}{\partial q} + \dot{\lambda}_{\mathrm{s}} \frac{\partial \varphi_{\mathrm{s}}}{\partial q} \tag{11}$$

where $\dot{\lambda}_{\mathrm{t}}, \dot{\lambda}_{\mathrm{s}}$ are the crack opening and sliding increments. The model is completed by the loading/unloading conditions of Kuhn-Tucker form:

$$\dot{\lambda}_i \geq 0, \quad \varphi_i \leq 0, \quad \dot{\lambda}_i \varphi_i = 0, \quad i = \mathrm{t,s} \tag{12}$$

The displacement jump, $\boldsymbol{\alpha}_d$, and the traction at the discontinuity, $\mathbf{t}_{\Gamma_d}$, fulfilling the Kuhn-Tucker conditions (12) are solved using the standard method of computational multi-surface viscoplasticity. Finally, the stress of an element with a discontinuity is computed as

$$\boldsymbol{\sigma} = \mathbf{E} : (\boldsymbol{\varepsilon}_{\mathrm{tot}} - (\nabla N^{sol} \otimes \boldsymbol{\alpha}_d)^{sym}) \tag{13}$$

This relation, where $\boldsymbol{\varepsilon}_{\mathrm{tot}}$ is the regular strain is, derived from (6) by (3). Then the traction vector for an element is given by $\mathbf{t}_{\Gamma_d} = \boldsymbol{\sigma} \cdot \mathbf{n}$.

### 2.4 Criteria for the Introduction of an Embedded Discontinuity and its Orientation

The Mohr–Coulomb (MC) and Rankine failure criteria are employed for indicating the introduction of new embedded discontinuities in the elements representing the intact rock material. These criteria are chosen due to their simplicity of implementation (both are linear in stresses and together they involve only three material parameters). Yet, they can predict the tensile and compressive failure (at low confinement levels) of many rocks with a reasonable accuracy (Goodman 1989; Jaeger and Cook 1971). In terms of principal stresses, these criteria are

$$f_{\mathrm{R}} = \sigma_1 - \sigma_{\mathrm{t}}$$
$$f_{\mathrm{MC}} = \frac{1+\sin\phi}{1-\sin\phi}\sigma_1 - \sigma_3 - \sigma_{\mathrm{c}} \tag{14}$$

where $\sigma_{\mathrm{c}}$ is the uniaxial compressive strength and $\varphi$ is the internal friction angle of rock material. The scheme for selecting the orientation of crack normal $\mathbf{n}$ is as follows:

$$\begin{aligned} &\text{If } f_{\mathrm{R}} > 0 \vee (f_{\mathrm{MC}} > 0 \wedge f_{\mathrm{R}} > 0) \\ &\quad \mathbf{n} = \mathbf{n}_1 \ (\text{or } \mathbf{n} = \mathbf{n}^+/h) \\ &\text{Elseif } f_{\mathrm{MC}} > 0 \wedge f_{\mathrm{R}} \leq 0 \\ &\quad \mathbf{n} = [-\sin\psi \quad \cos\psi]^T \end{aligned} \tag{15}$$

Thereby, the crack normal is orthogonal to the first principal direction, $\mathbf{n}_1$, or reoriented according to Eq. (8), if Rankine criterion is violated. If only MC criterion is violated, the orientation of the crack plane is based on MC analysis, as $\psi = \pi/4 + \phi/2$. Finally, it should be emphasized that all embedded discontinuities can open in both modes I and II irrespective of the mechanism, i.e. a violation of the Rankine or MC criterion, through which they are introduced.

### 2.5 Solving the Equations Governing the Problem

The governing equations of motion are solved with the explicit time integrator. Accordingly, the solution process including the determination of the displacement jump is as follows. First, the present displacement, $\mathbf{u}_t$, is utilized in solving the local, element level problem for the present value of displacement jump $\boldsymbol{\alpha}_{d,t}$ with the method presented in Sect. 2.3. Then, the stress is calculated with Eq. (13) after which the internal force vector is computed for each element and assembled in the standard manner for the whole system of equations. Finally, the response is computed further in time with the selected integration scheme. It is emphasized that with the present EAS-based approach, no kinematical continuity between the discontinuity lines of neighboring elements is imposed. This means that the macro discontinuity line consisting of the displacement discontinuities of single elements can be interpreted as a dominant crack direction. The present method can represent a single crack line without locking, as shown in numerical simulations by Brancherie and Ibrahimbegovic (2009).

The explicit modified Euler method is chosen for time integration. It is a second order method (in convergence) having the same critical time step as the central difference scheme (Hahn 1991). The system response is calculated as

$$\begin{aligned} \ddot{\mathbf{u}}_t &= \mathbf{M}^{-1}\left(\mathbf{f}_t^{\mathrm{ext}} - \mathbf{f}_t^{\mathrm{int}}\right) \\ \dot{\mathbf{u}}_{t+\Delta t} &= \dot{\mathbf{u}}_t + \Delta t \ddot{\mathbf{u}}_t \\ \mathbf{u}_{t+\Delta t} &= \mathbf{u}_t + \Delta t \dot{\mathbf{u}}_{t+\Delta t} \end{aligned} \tag{16}$$

where $\Delta t$ is the time step and $\mathbf{f}_t^{\mathrm{int}}$, $\mathbf{f}_t^{\mathrm{ext}}$ are the internal and external force vector, respectively.

### 2.6 Rock Heterogeneity and Initial Microcrack Population Description

Rock heterogeneity is incorporated in the present approach with the method by Mahabadi et al. (2010). In this method, the mechanical properties and percentages of the constituent minerals of a given rock are needed. The method to describe the mineral texture is as follows. First, a finite element mesh with an average element size (preferably corresponding to the average rock grain size) is generated. Now, assume that the given rock has 3 different minerals with percentages 60 % (mineral 1), 30 % (mineral 2) and

10 % (mineral 3). Then, an array consisting of material property set numbers 1, 2 and 3 with a length equal to the number of elements in the mesh is generated. The amount of these numbers in the array is the same as the percentage of corresponding minerals in the rock. Finally, this array is randomly shuffled and mapped into the mesh so that a spatially random distribution of mineral property sets is obtained.

As for the initial microcrack population description, it is modeled as randomly oriented embedded discontinuities. First, an array with length $N_{ele}$ (number of elements in the mesh), having 1 as an entry if the element corresponding to that entry contains an initial microcrack and 0 otherwise, is generated. The amount of entries with ones (corresponding to the number of microcracks) is a parameter. This array is randomly shuffled in order to obtain spatially random distribution of microcracks. Then, a randomly oriented (the crack normal vector alignment being evenly distributed between 0 and $\pi$) embedded discontinuity is assigned for each element designated as containing a microcrack. The strength parameters of these discontinuities are set close to zero, i.e. they open in both modes without much resistance. These techniques are illustrated in the numerical simulations.

## 3 Numerical Simulation: Results and Discussions

Numerical simulations demonstrating the performance of the present model are carried out in this section. Model predictions are demonstrated at the structural level in simulation of uniaxial compression and tension. The effects of the model and parameters as well as mesh element size are tested therein. Finally, the effects of strain rate and confinement are tested. All simulations are carried out in 2D case under the plane strain assumption.

### 3.1 Effect of Initial Crack Population and Heterogeneity in Uniaxial Compression

Uniaxial compression test is simulated in this section to demonstrate the characteristics of the model response and test the influence of different model components. The CST mesh with the boundary conditions is depicted in Fig. 3a. Confining pressure, $\sigma_{conf}$, is set to zero here. Standstead granite is chosen as the rock material. Its constituent minerals along with their properties and percentages in the specific sample examined by Mahabadi (2012) are given in Table 1.

Table 1 also gives the equivalent homogeneous values based on the percentages of the mineral interfaces in the sample (Mahabadi 2012). It should be mentioned that there is a considerable discrepancy in the mechanical properties of the three minerals given in the literature, see e.g. (Mahabadi 2012; Liu et al. 2004b; Li et al. 2003). Furthermore, the cohesion values are modified by multiplying the original ones by factor of 2 to obtain more realistic (i.e. better matching the experiments in Mahabadi (2012)) results with the present model.

Elastic limits in tension and shear of the present model, $\sigma_t$, $\sigma_s$, are identified with the tensile strength and the modified cohesion values of the minerals given here. Thus, the reason for the need to modify the original values of cohesion in Table 1 is that the elastic shear limit of a discontinuity line (microcrack) in the present model is a material point level property while the values of cohesion are based on the laboratory sample scale. Moreover, the modified values are closer to the shear strength values 55.2 MPa and 55.1 MPa for Inada granite and Stone Mountain granite, respectively, reported in (Goodman 1989). The uniaxial compressive strength in the MC criterion (14) is related to the cohesion as $\sigma_c = 2\cos\varphi/(1-\sin\varphi)c_0$.

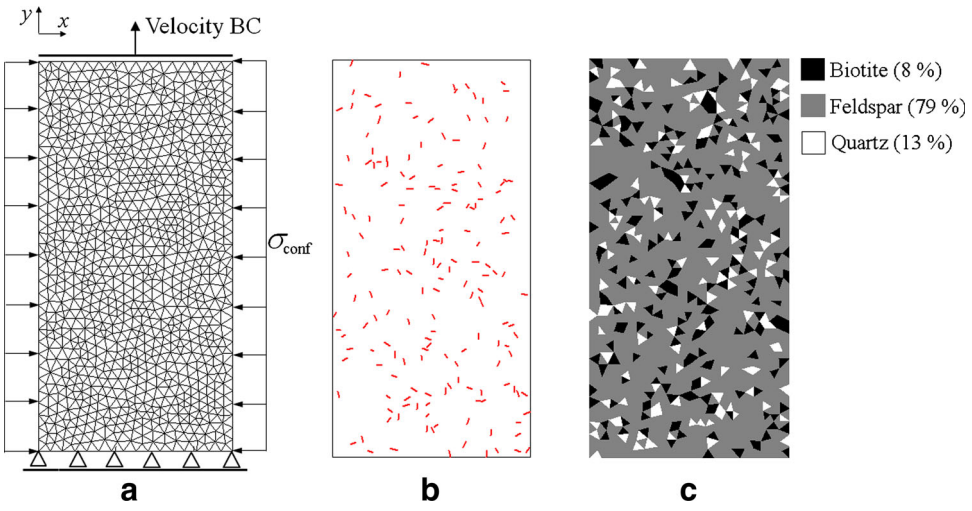


**Fig. 3** CST-mesh (1738 elements) and boundary conditions for the simulations (dimensions of the specimen are 25 × 25 × 50 mm) (**a**), initial microcrack population (10 % of the elements contain a crack) (**b**) and the numerical representation of microstructure (**c**)

**Table 1** Material properties for the minerals of Standstead granite and equivalent homogeneous values [after (Mahabadi 2012)]

| Parameter | Quartz | Feldspar | Biotite | Homogeneous |
|---|---|---|---|---|
| $\rho$ (Density) (kg/m$^3$) | 2,600 | 2,600 | 2,800 | 2,616 |
| $E$ (Elastic modulus) (GPa) | 80 | 70 | 20 | 67.3 |
| $v$ (Poisson's ratio) | 0.17 | 0.29 | 0.20 | 0.27 |
| $\sigma_t$ (Tensile strength) (MPa) | 10 | 10 | 7 | 8.9 |
| $c_0$ (Cohesion) (MPa) | 50* | 50* | 50* | 45.8* |
| $\varphi$ (Internal friction angle) | 50° | 50° | 50° | 47.4° |
| $G_{Ic}$ (Mode I fracture energy) (J/m$^2$) | 40 | 40 | 28 | 35.5 |
| Percentage in the sample | 13 % | 79 % | 8 % | 100 % |

* The original values are 25 MPa for minerals and 22.9 MPa for the homogeneous case

The initial microcrack population with random orientation of cracks and 10 % of elements having a crack is shown in Fig. 3b. As the average element size is 1.56 mm in the mesh, it is also the average length of the initial microcracks. However, it should be kept in mind that the length of the discontinuity line does not appear explicitly in the present formulation. The strengths, (i.e. the elastic limits) of the initial microcracks are set close to zero so that they open without significant resistance. Figure 3c displays the heterogeneity description generated with the method described in Sect. 2.6.

All simulations are carried out using a constant velocity boundary condition with $v = 0.1$ m/s and viscosity modulus value $s = 0.001$ MPas/m if not otherwise explicitly stated. This viscosity value is low enough so that no strain rate effects can be observed at the prescribed boundary velocity. In the first simulation, the orientation of the embedded discontinuity is perpendicular to the first principal direction, i.e. $\mathbf{n} = \mathbf{n}_1$. The results of the simulation are presented in Fig. 4. The loading induced microcrack distributions and the magnitude of displacement jumps are plotted therein, and in all simulations results shown hereafter, at different stages of the loading process. These stages are indicated by arrows attached to the axial stress–strain curves. The stress–strain curves are plotted with the usual convention in geomechanics, i.e. compressive quantities are positive. The axial, lateral and volumetric strains in Fig. 4 are average values approximated, respectively, by

$$\begin{aligned} \varepsilon_{\text{axial}} &= (\underbrace{\bar{u}^{y,t}_{\text{bottomedge}}}_{=0} - \bar{u}^{y,t}_{\text{topedge}})/h \\ \varepsilon_{\text{lateral}} &= (\bar{u}^{x,t}_{\text{leftedge}} - \bar{u}^{x,t}_{\text{rightedge}})/b \\ \varepsilon_{\text{vol}} &= \varepsilon_{\text{axial}} + 2\varepsilon_{\text{lateral}} \end{aligned} \tag{17}$$

where $h$ and $b$ are the height and width of the numerical specimen, respectively, while $\bar{u}^{x,t}_{\text{leftedge}}$ and $\bar{u}^{x,t}_{\text{rightedge}}$ are the average nodal displacements in the $x$-direction of the left and right edges of the sample at time $t$, and $\bar{u}^{y,t}_{\text{bottomedge}}$, $\bar{u}^{y,t}_{\text{topedge}}$ are corresponding displacements in y-direction of the bottom and top edges.

It can be observed from the results in Fig. 4a that Mode I (Rankine) fracture events start quite early during the loading process. All these events occur at the elements adjacent to elements with initial microcracks. Moreover, at the end of the loading process most of the elements in the mesh have a crack, either initial, Rankine or MC type. Some of these cracks open significantly more than others so as to form localization patterns (Fig. 4e–g) that can be interpreted as macrocracks. These cracks clearly form typical axial (vertical) or slightly-aligned cracks. The corresponding stress–strain curves in Fig. 4h have similar characteristics as observed in the experiments for many rocks (Jaeger and Cook 1971). In particular, the post-peak part of the axial stress–strain curve becomes steeper as the strain increases. This behavior indicates a loss of stability of the sample. Thus, this behavior could be interpreted as the brittle intragranular fracture of single grains discussed by Pininska (2008) (see also Introduction). The volumetric strain is first compacting in nature and then, as more cracks initialize and open, becomes dilatant.

As for the microcracks introduced by a violation of the MC criterion (the inclination of these cracks is 70° referencing to $x$-axis), they are very few. The reason for this is that the uniaxial compressive strength of all the minerals is so high ($\approx$274 MPa) that the numerical sample fails, due to the weakening effect of initial microcracks, before the element stresses reach (the peak stress is circa 82 MPa) the UCS of the minerals. The influence of the cohesion will be tested later in Sect. 3.2.3. If the initial microcrack population is neglected, the results shown in Fig. 5 are obtained (keeping the mineral description unaltered).

The amount of microcracks introduced by violation of the MC criterion is considerably larger in the simulation without the initial microcrack population, as can be observed in Fig. 5c. These cracks localize forming macroscopic shear bands, as attested in Fig. 5d. However, most of the cracks here are of Rankine type. These cracks initialize due to the heterogeneity of the material and form long axial cracks reaching the bottom edge of the sample (Fig. 5e) at the end of the failure process. The resulting final failure mode is quite different from that produced with the presence of initial microcrack population. Furthermore, the peak stress, 160 MPa, is twice as high as it was in the simulation with the initial microcracks and the pre-peak parts of the stress–strain curves are more linear here.

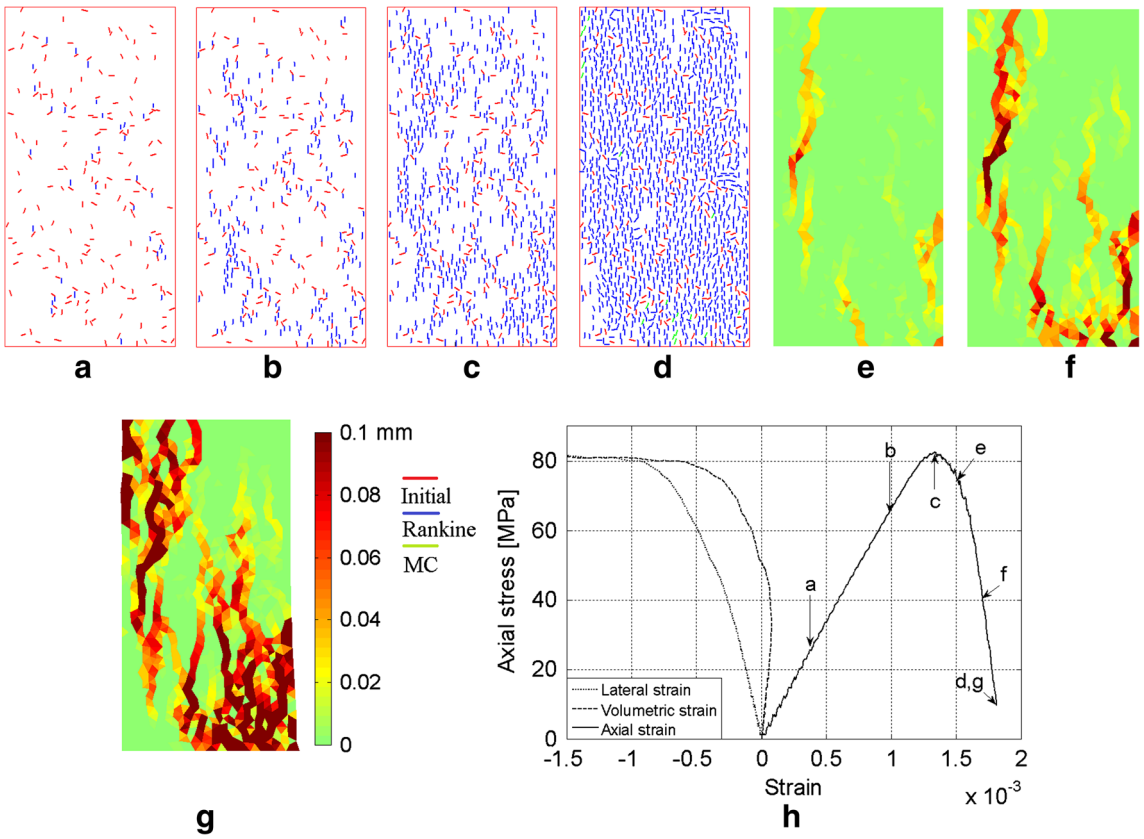


**Fig. 4** Simulation results (initial microcrack population, heterogeneous material): Initial (*red bars*) and loading-induced microcrack (*blue* and *green bars*) distributions (**a**)–(**d**) and magnitude of displacement jumps (**e**)–(**g**), and corresponding stress–strain curves (**h**)

As a final simulation of this section, the heterogeneity description is neglected and the simulation is repeated with the homogeneous material properties given in Table 1. The results are shown in Fig. 6.

The results from the simulation with homogeneous material (see Fig. 6) differ from the heterogeneous counterpart (see Fig. 4) in details only. Here the final failure mode has, however, more damage in the right lower corner of the specimen. Therefore, in the present numerical approach the presence of the initial microcrack population has a more substantial influence on the resulting failure patterns and the stress–strain response than the heterogeneity description. The mineral values given in Table 1, however, do not differ severely from each other which partly explain this finding. Indeed, the cohesion and friction angle are equal for all the minerals and the tensile strength of Biotite is 70 % of that for Quartz and Feldspar (both 10 MPa). This may explain why the present heterogeneity description does not affect the compressive strength of the numerical sample. These numerical modeling related findings may have their representations in reality. It is, nonetheless, beyond the scope of the present study (concentrating on model development) to consider these experimental issues in more detail.

### 3.2 Effect of Microcrack Orientation in Uniaxial Compression

The alternative orientation scheme for the tensile microcrack according to Eq. (8) is tested in this section. The simulation with the initial microcrack population and microstructure shown in Fig. 3 are repeated here. The results are shown in Fig. 7.

When the orientation of mode I microcracks is according to Eq. (8), the macrocracks seem to be more aligned than in the case when microcracks are orthogonal to the first principal direction. First such macrocracks, shown in Fig. 7d, are formed as a consequence of many mode I microcracks linking together. The peak stress of the stress–strain response is lower here than in the simulation with orthogonal cracks. Moreover, the post-peak part of the curve is less steep indicating a more stable failure process. These differences are clearly related to the alignment of mode I cracks which facilitate sliding, i.e. mode II opening, of the cracks. This orientation scheme also adds an extra source of randomness to the model when nonstructured meshes are used.

The failure process with this orientation scheme represents thus, to some extent, the intergranular microcracking

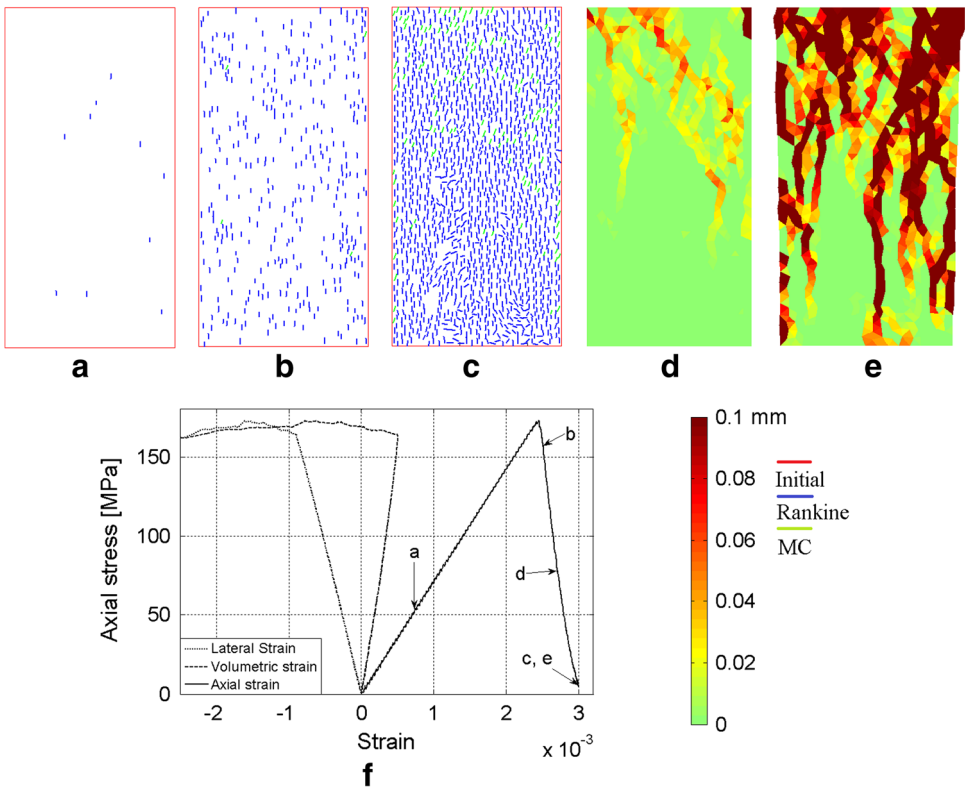


**Fig. 5** Simulation results (no initial microcrack population, heterogeneous material): Loading-induced microcrack distributions (**a**)–(**c**) and magnitude of displacement jumps (**d**), (**e**) at different stages of the loading process, and corresponding stress–strain curves (**f**)

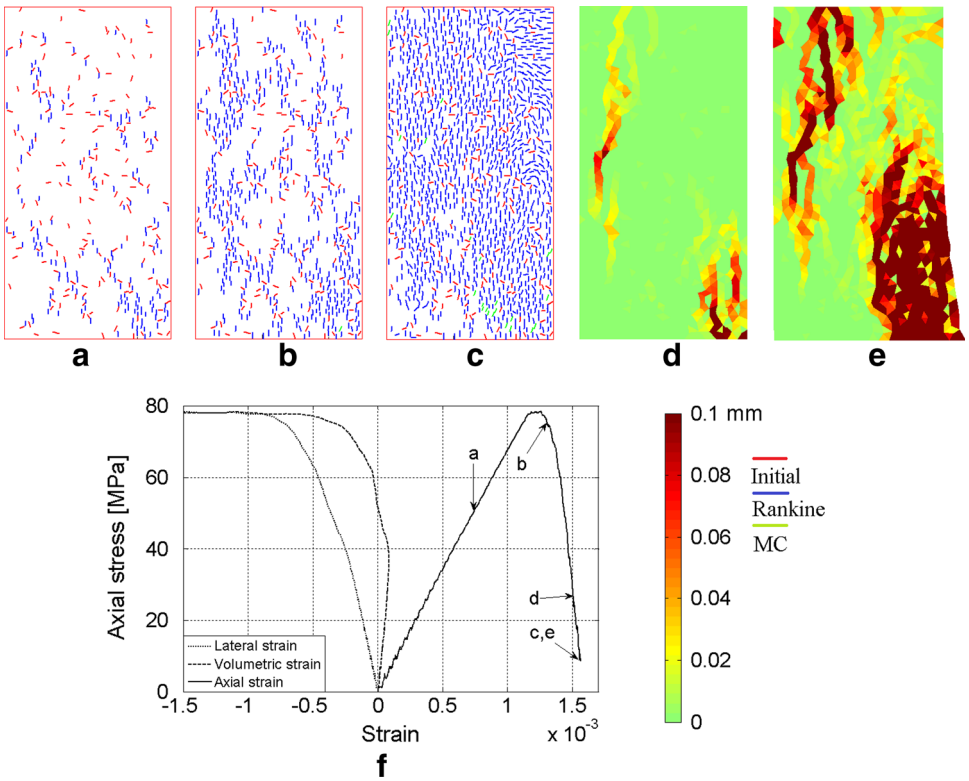


**Fig. 6** Simulation results (initial microcrack population, homogeneous material): Initial and loading-induced microcrack distributions (**a**)–(**c**) and magnitude of displacement jumps (**d**), (**e**) at different stages of the loading process, and corresponding stress–strain curves (**f**)

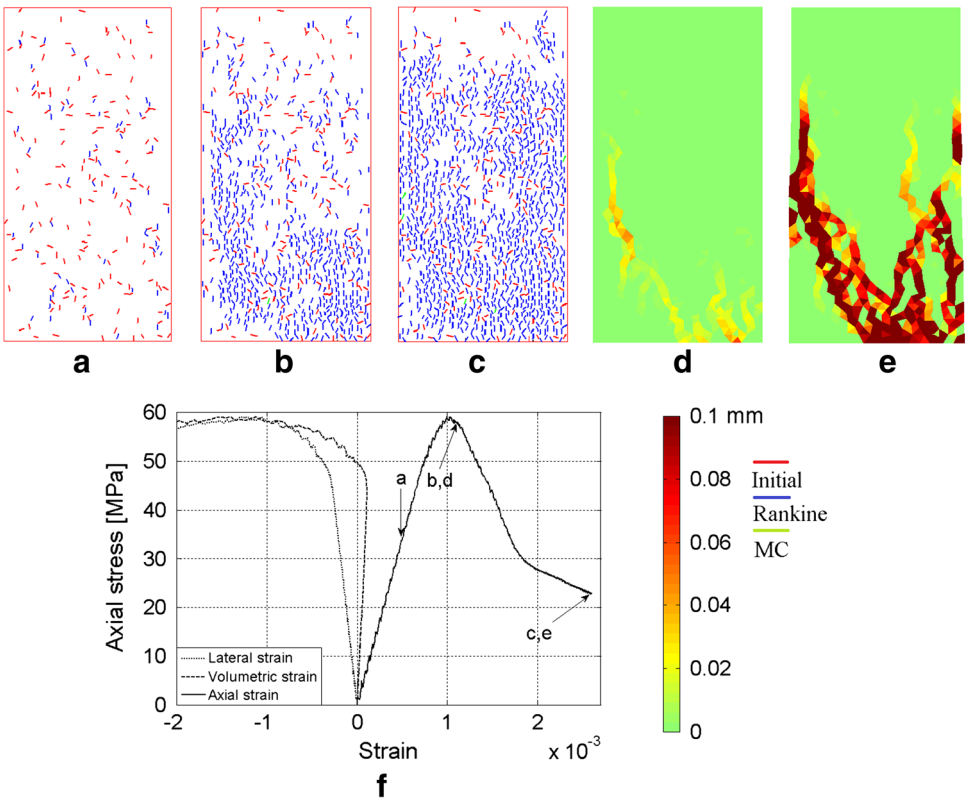


**Fig. 7** Simulation results when tensile microcrack is parallel to one of the sides of the triangle (initial microcrack population, heterogeneous material): Microcrack distributions (**a**)–(**c**) and magnitude of displacement jumps (**d**), (**e**) at different stages of the loading process, and corresponding stress–strain curves (**f**)

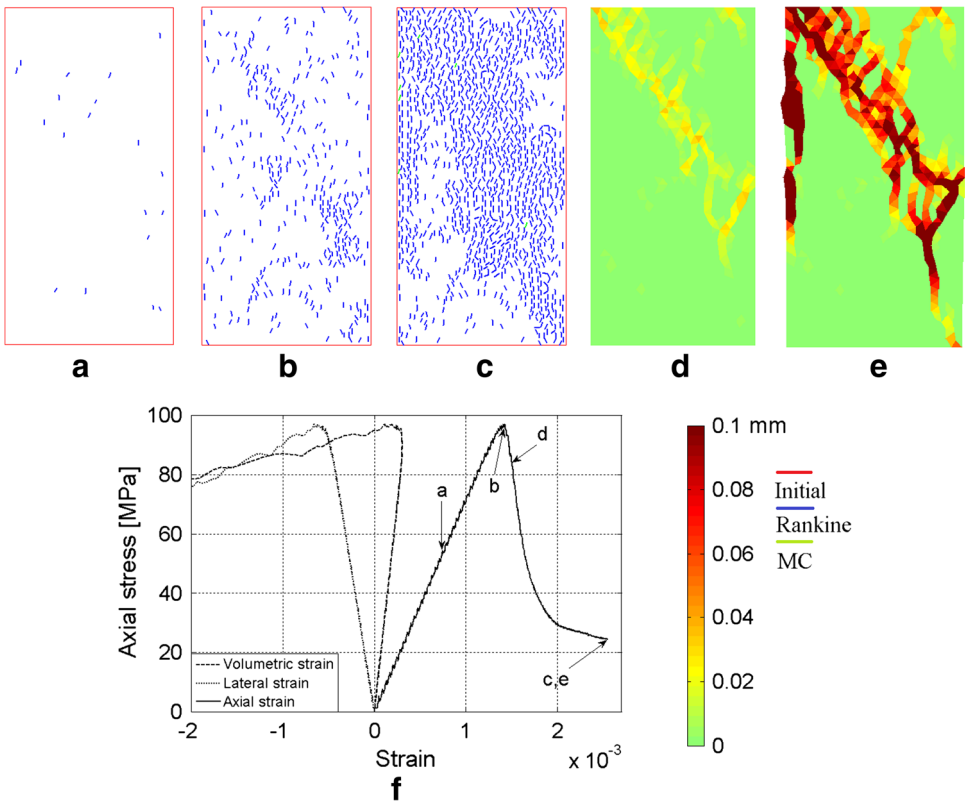


**Fig. 8** Simulation results when tensile microcrack is parallel to one of the sides of the *triangle* (no initial microcrack population and heterogeneous material): Microcrack distributions (**a**)-(**c**) and magnitude of displacement jumps (**d**), (**e**) at different stages of the loading process, and corresponding stress–strain curves (**f**)

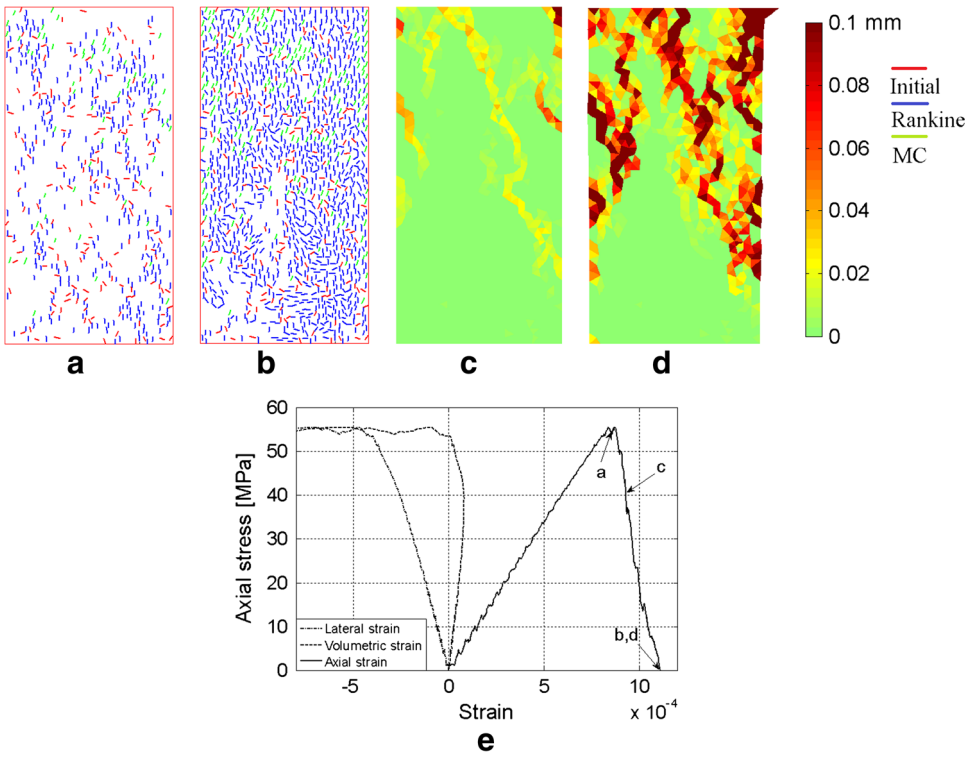


**Fig. 9** Simulation results with $\sigma_s = 25$ MPa (initial microcrack population, heterogeneous material): Microcrack distributions (**a**), (**b**) and magnitude of displacement jumps (**c**), (**d**) at different stages of the loading process, and corresponding stress–strain curves (**e**)

of carbonate and soft rocks, discussed by Pininska (2008) (see also "Sect. 1"), leading to a more shear dominated fracture process.

Next, the simulation is carried out without the initial microcrack population. The results are shown in Fig. 8.

Without the initial microcrack population, a thick shear band formed by coalescing mode I microcracks spans the sample from the left upper corner to the right lower corner. Moreover, the peak stress is again considerably higher than in the simulation with the initial microcrack population.

### 3.3 Influence of Shear Strength Parameter in Uniaxial Compression

The present discontinuity model decomposes the displacement jump into separate components corresponding to mode I (opening) and mode II (sliding). Therefore, it is to be expected that the mode II elastic limit, i.e. the shear strength parameter, has a substantial influence on the model behavior in compression. For this reason, the simulation with the initial microcrack population and heterogeneous material is first repeated here with the original cohesion values given in (Mahabadi 2012), i.e. the shear elastic limit is set as $\sigma_s = 25$ MPa. Results are shown in Fig. 9.

The failure response with the lowered shear strength of 25 MPa is quite different indeed from that predicted with the modified value of 50 MPa, as observed on comparing Figs. 4 and 9. The peak stress is here considerably lower (circa 55 MPa) and the post-peak part of the axial stress–strain curve has the opposite features to the curve in Fig. 4. One reason for the differences is the larger amount of cracks introduced via violation of the MC criterion which leads in a more stable failure process.

Next, a higher value of shear strength parameter is tested. Results from a simulation with $\sigma_s = 100$ MPa are shown in Fig. 10.

When the shear strength is 100 MPa, there are very few cracks introduced by the violation of the MC criterion and the macrocracks are more axial than in the simulations with lower shear strengths (see Fig. 10c). Moreover, the pre-peak part of axial stress–strain curve exhibits a clear bent at the stress level of 55 MPa. The reason for this is the formation of a long axial crack spanning the whole specimen shown in Fig. 10c. This long axial crack becoming more and more apparent from Fig. 9 ($\sigma_s = 25$ MPa) and Fig. 4 ($\sigma_s = 50$ MPa) to Fig. 10 ($\sigma_s = 100$ MPa), is due to increasing shear strength.

### 3.4 Influence of Randomness of Heterogeneity and Initial Microcrack Population

All the previous simulations have been performed using the same microstructure and initial microcrack population shown in Fig. 3. In this section the effect of random generation both the microstructure and the initial microcrack population is demonstrated. Three different simulations with individual heterogeneity and initial microcrack descriptions in each are carried out. The percentage of

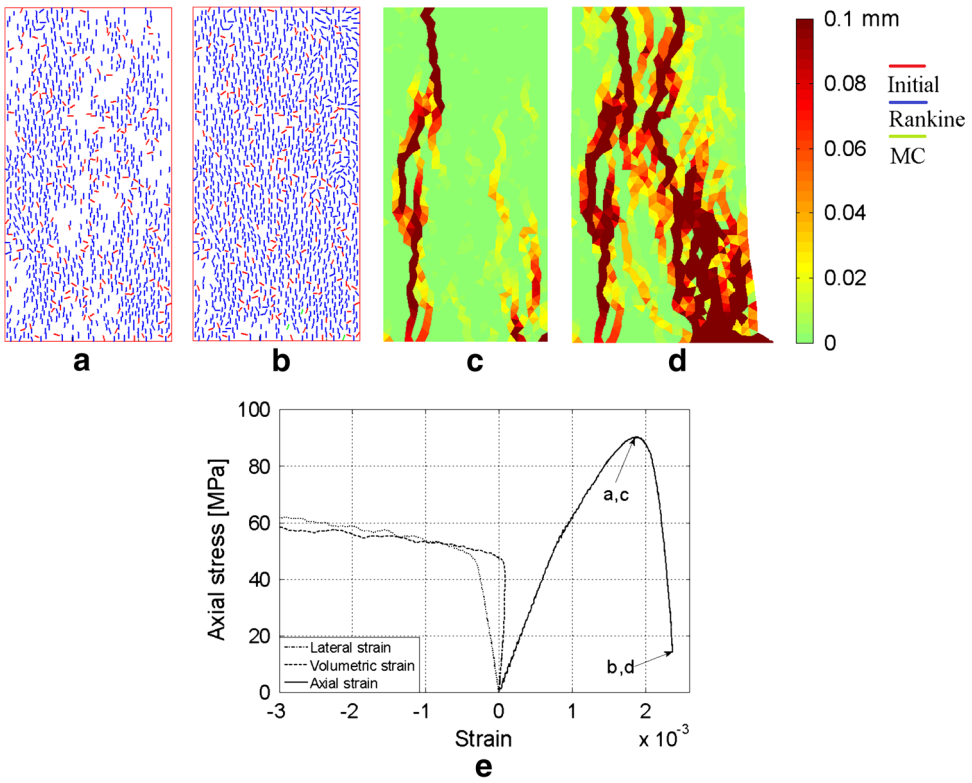


**Fig. 10** Simulation results with $\sigma_s = 100$ MPa (initial microcrack population, heterogeneous material): Microcrack distributions (**a**),(**b**) and magnitude of displacement jumps (**c**), (**d**) at different stages of the loading process, and corresponding stress–strain curves (**e**)

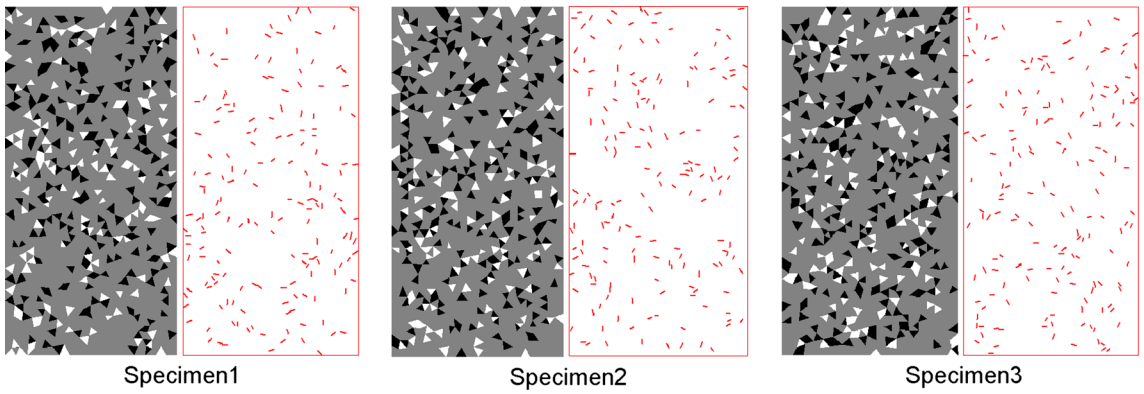


**Fig. 11** Numerical specimens for demonstration of the influence of randomness of microstructure and initial microcrack population

elements with an initial microcrack and the constituent mineral percentages are kept unaltered.

The numerical specimens are shown in Fig. 11 and the results from the simulations with these specimens are plotted in Fig. 12.

The final failure modes shown in Fig. 12, while differing in details, have quite similar general characteristics but the axial stress–strain curves deviate considerably. Particularly, Specimen3 has about 24 % higher strength (105 MPa) than Specimen1 and Specimen2 which both have the strength of circa 85 MPa. Moreover, while the post-peak softening behavior of Specimen1 and Specimen3 is similar, Specimen2 displays a significantly more ductile response. Thus, even this highly limited sample of three specimens seems to demonstrate that the present approach can replicate, at least to some extent, the vast deviations in the compressive strength data for different rocks in the literature.

### 3.5 Influence of Mesh Density in Uniaxial Compression

The effect of the element size is tested in this section. For this end, a CST mesh with an average side length of 1 mm is generated resulting in 4276 triangles. In addition, the percentage of elements containing an initial microcrack is

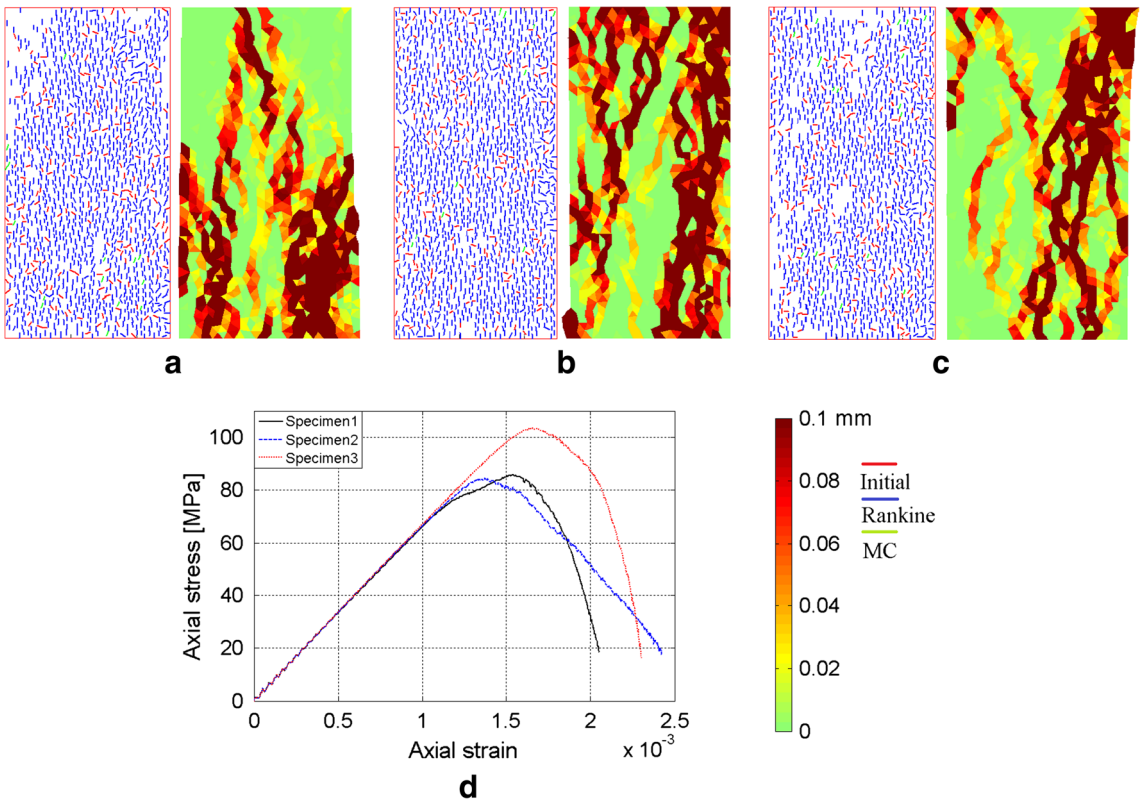


**Fig. 12** Simulation results with the numerical specimens (initial microcrack population, heterogeneous material): Microcrack distributions and magnitude of displacement jumps at the end of failure process for Specimen1 (**a**), Specimen2 (**b**), Specimen3 (**c**) and corresponding stress–strain curves (**d**)

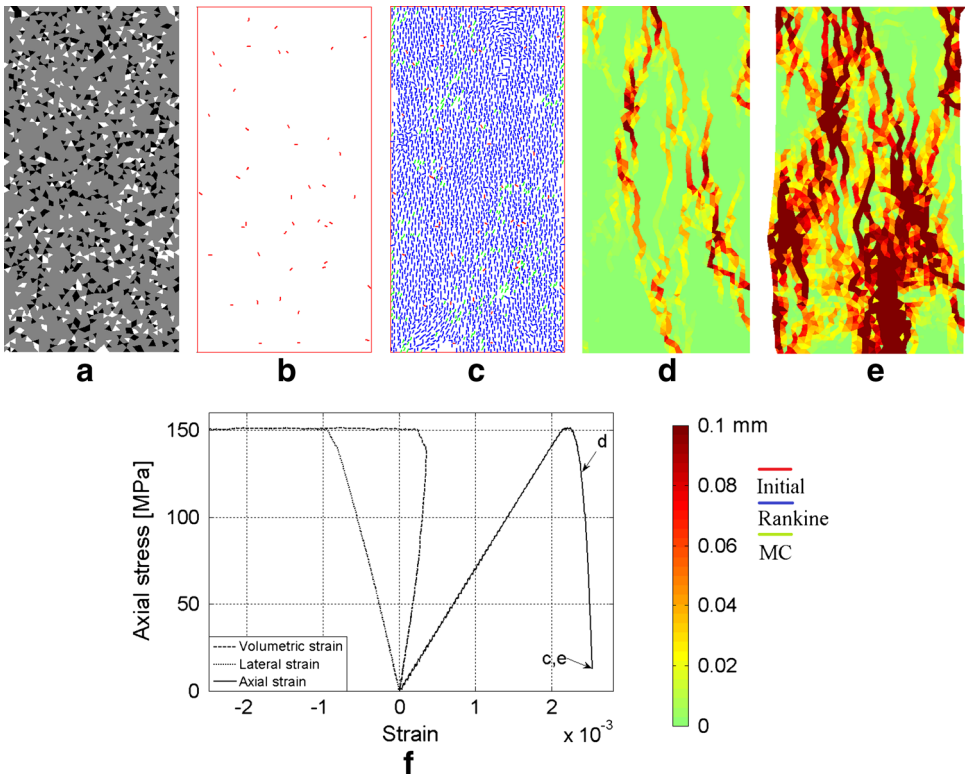


**Fig. 13** Simulation results with a denser mesh (initial microcrack population, heterogeneous material): Mineral distribution (**a**), initial microcrack distribution (**b**), microcrack distribution at the end of loading process (**c**) magnitude of displacement jumps at different stages of the failure process (**d**), (**e**), and corresponding stress–strain curves (**f**)

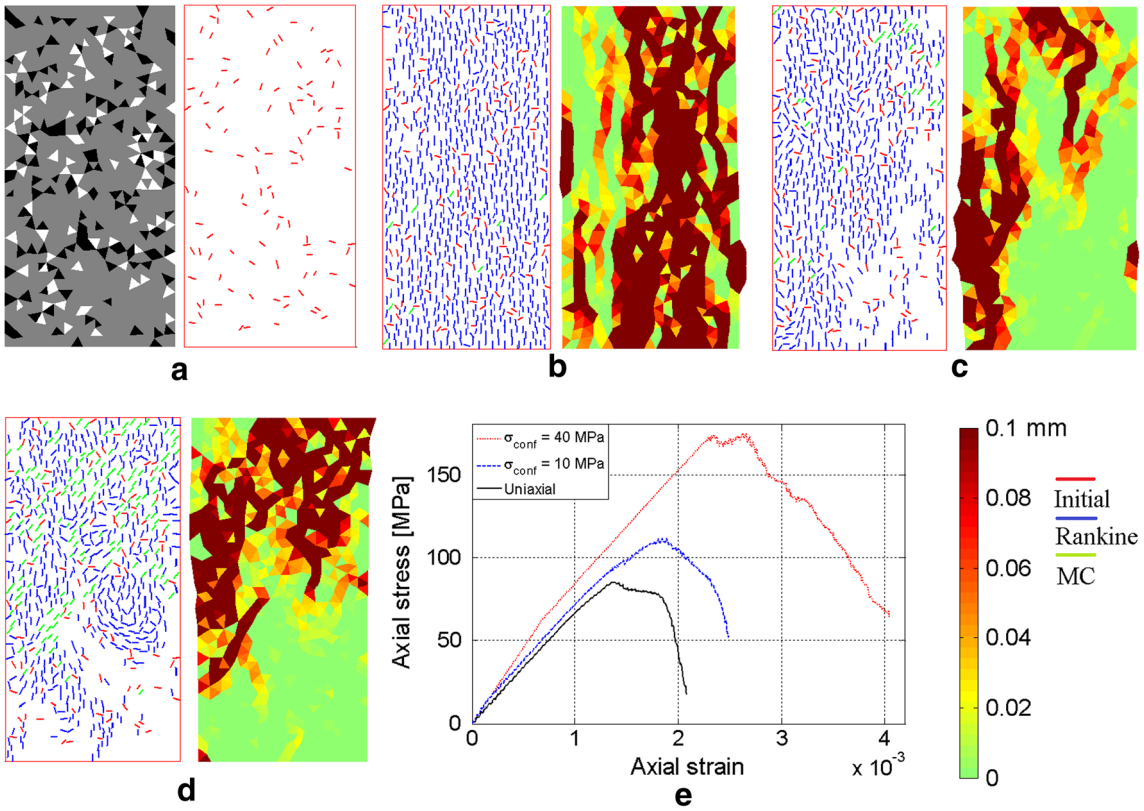


**Fig. 14** Influence of confining pressure ($\mathbf{n} = \mathbf{n}_1$, initial microcrack population, heterogeneous material): Numerical specimen (**a**), final microcrack distribution and magnitude of displacement jumps in uniaxial (**b**), $\sigma_{\text{conf}} = 10$ MPa (**c**), $\sigma_{\text{conf}} = 40$ MPa (**d**) case, and corresponding stress–strain curves (**e**)

set to 1 %. The other data and parameters are as in the first simulation. The results are shown in Fig. 13.

The general characteristics of results are the same as with the coarser mesh. Some of the microcrack openings localize so as to form axial macrocracks, as observed in Fig. 13d. Here the peak strength, ∼150 MPa, is higher than that with the coarser mesh due to fewer initial microcracks. This simulation shows that the present model can be calibrated so as to match the experimental results of real rocks (Standstead granite in this case with UCS of 147.3 MPa reported in Mahabadi (2012)). This calibration does not necessarily require changing the mesh density but the material and model parameters. However, the element size should be small enough so that the heterogeneity and microcrack distributions of the rock can be realistically represented. Small element size unfortunately leads to computationally more costly simulations.

### 3.6 Influence of Confining Pressure in Compression

The effect of confining pressure is tested in this section. A coarser mesh with the average side length of 2 mm (resulting in 1052 elements) is used for this end to save computational time. Both mode I crack orientation options are tested. Moreover, the same numerical specimen is used at each levels of confinement despite the fact that this is never the case in reality. Confining pressure is applied gradually so that it increases with the same rate as the compressive axial stress due the constant velocity boundary condition (see Fig. 3). After reaching the prescribed value, the confining pressure is kept fixed while the axial compression still increases. The numerical specimen used in all simulations in this section and the results for the orientation scheme $\mathbf{n} = \mathbf{n}_1$ are shown in Fig. 14.

Based on the results in Fig. 14, the effect of confining pressure is that it suppresses the tensile (mode I) cracking which in turn results in an increase of the shear (mode II) microcracks as the ability of the specimen to bear load increases under higher confinement. The resulting final failure mode becomes more shear-dominated at higher levels of confinement (see Fig. 14c). Furthermore, the response becomes more ductile as the confining pressure increases (see Fig. 14e).

Next, the optional mode I crack orientation scheme is tested while the MC type of microcrack initiation is neglected. Results are shown in Fig. 15.

In the simulations with the alternative mode I crack orientation scheme and the absence of MC cracks, the axial

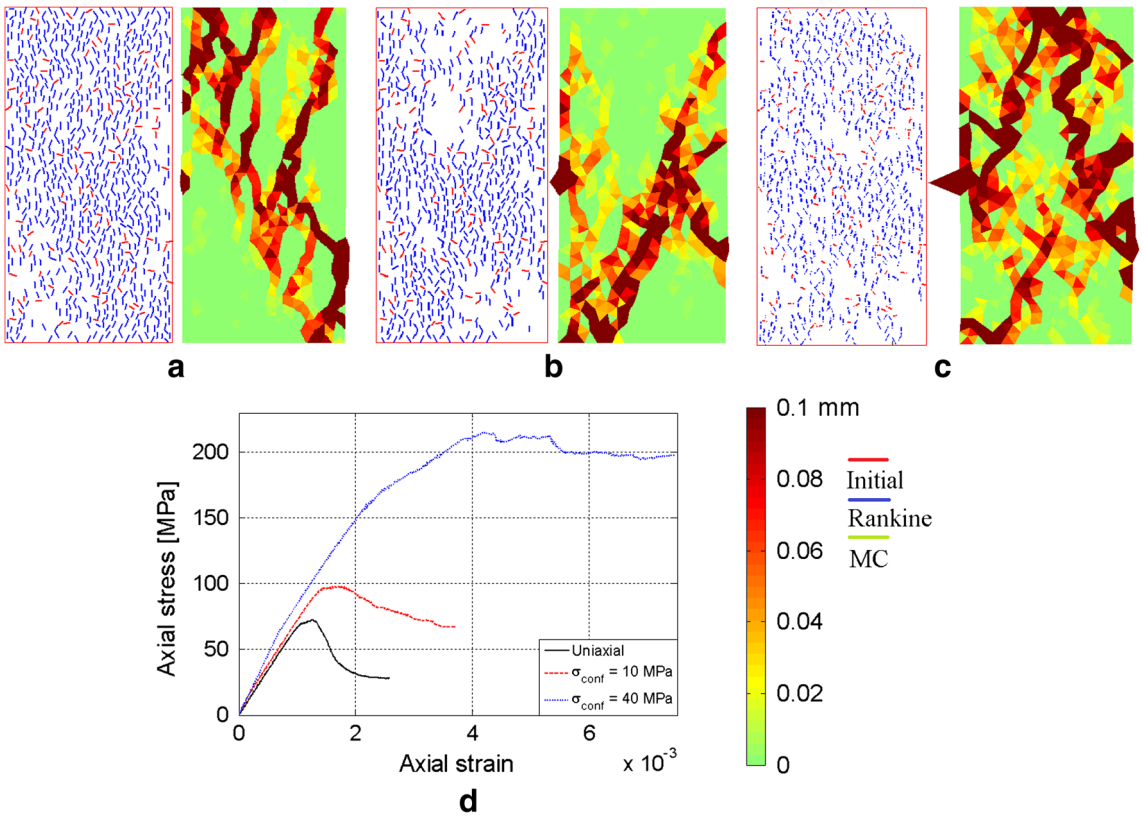


**Fig. 15** Influence of confining pressure ($\mathbf{n} = \mathbf{n}^{+}/h$, initial microcrack population, heterogeneous material, no MC cracks): Final crack distribution and magnitude of displacement jumps in uniaxial (**a**), $\sigma_{\text{conf}} = 10$ MPa (b), $\sigma_{\text{conf}} = 40$ MPa (**c**) case, and corresponding stress–strain curves (**d**)

macrocracks generated in the unconfined case (Fig. 15a) are suppressed and a major shear band spanning the specimen diagonally is formed at level 10 MPa of confinement (see Fig. 15b). At the highest level of confinement, 40 MPa, the failure mode is quite messy. In addition, it can be observed that the response becomes increasingly ductile as the confining pressure increases. The stress–strain curve corresponding to 40 MPa of confining pressure displays very little softening. Thereby, the confining pressure-dependent brittle-to-ductile transition observed in the experiments with compact carbonate rocks such as limestone and marble (Wei and Anand 2008; Paterson 1958), could be captured with the present model. It would be beneficial in this regard to describe the bulk material with Mohr–Coulomb or Drucker-Prager plasticity model so as to incorporate the grain interior plasticity.

### 3.7 Influence of Loading Rate in Uniaxial Compression

As the present model incorporates the strain rate dependency via viscosity, its influence on the specimen response should be tested. Thereby, uniaxial compression described in Fig. 3 using the material properties given in Table 1 is simulated here. First, the effect of higher loading rate is tested setting the boundary velocity to be $v_0 = -0.5$ m/s (viscosity is kept unaltered, i.e. $s = 0.001$ MPas/m). Then higher value of viscosity modulus, $s = 0.005$ MPas/m is tested with the original velocity $v_0 = -0.1$ m/s. Results are shown in Fig. 16.

The influence of higher loading rate is in accordance with the experiments (Zhang and Zhao 2014), i.e. the peak-stress increases (from 82 MPa in Fig. 4 to almost 115 MPa here) and response becomes more ductile as more cracks are initiated and, consequently, more energy is dissipated. Almost identical effect is produced, with the present model, by increasing the viscosity modulus while keeping the loading rate fixed (compare Fig. 16d, e). Finally, it is noted that the oscillation in the stress–strain curve with the higher velocity (blue curve in Fig. 16f) is caused by the initial velocity condition $v(t = 0\ \text{s}) = -0.5$ m/s which generates a stress wave that propagates back and forth between the specimen top and bottom edges.

### 3.8 Response in Uniaxial Tension

Finally, the model prediction is demonstrated in uniaxial tension, at the structural level, with the problem setup illustrated in Fig. 3 with the exception that the boundary

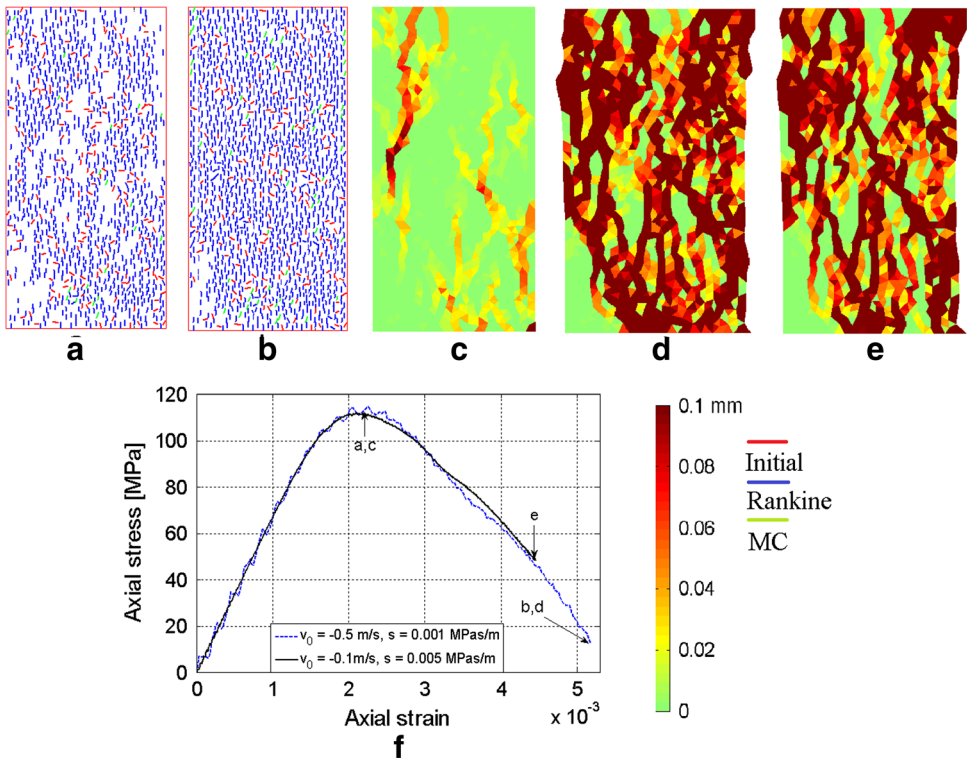


**Fig. 16** Influence of loading rate and viscosity (initial microcrack population, heterogeneous material): Microcrack distributions (**a**), (**b**) and magnitude of displacement jumps (**c**), (**d**) at different stages of loading process when $v_0 = -0.5$ m/s, $s = 0.001$ MPas/m, and the magnitude of displacement jumps at the end of loading process (**e**) when $v_0 = -0.1$ m/s, $s = 0.005$ MPas/m, and corresponding stress–strain curves (**f**)

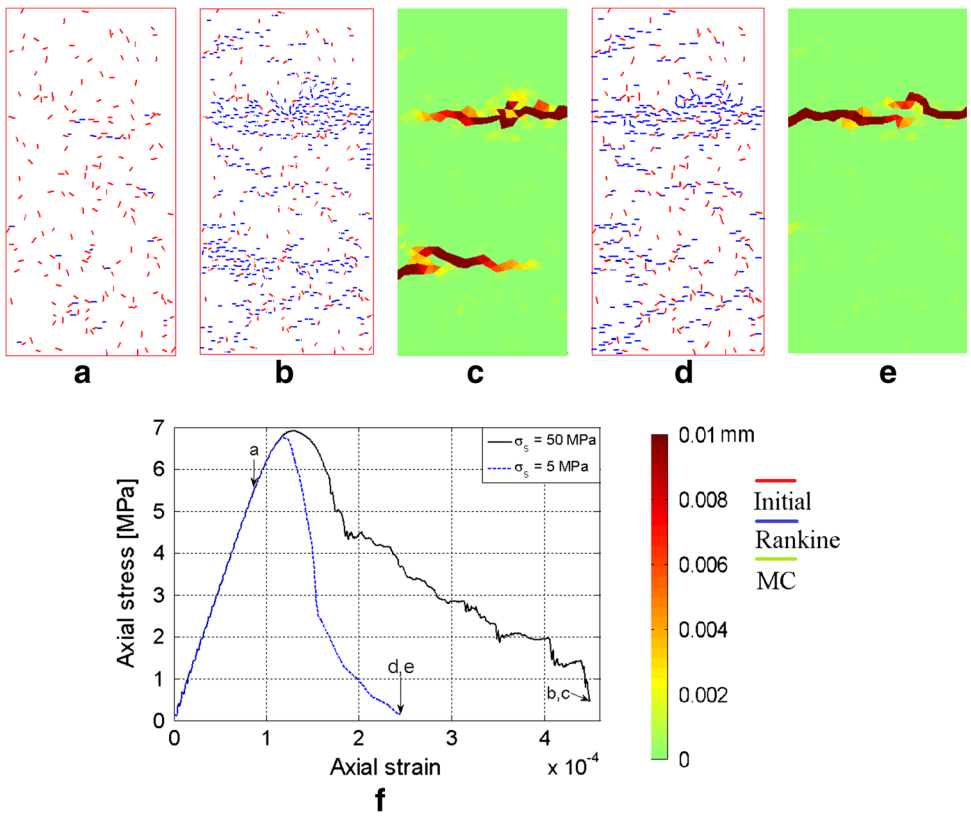


**Fig. 17** Simulation results for uniaxial tension test (initial microcrack population, heterogeneous material): Microcrack distributions (**a**),(**b**) and magnitude of displacement jumps (**c**) at different stages of loading process when $\sigma_s = 50$ MPa, and microcrack distribution and magnitude of displacement jumps at the end of loading process (**d**), (**e**) when $\sigma_s = 5$ MPa, and corresponding stress–strain curves (**f**)

velocity is set now to $v_0 = 0.01$ m/s (other data is unaltered). Results from two simulations with $\sigma_s = 50$ MPa and $\sigma_s = 5$ MPa are shown in Fig. 17. The latter 10 times smaller value is chosen just for demonstrational purposes.

It can be observed that while there is no significant deviation in the peak stresses, the post peak behavior and the resulting failure mode differ substantially. Particularly, the low shear strength of microcracks leads to a more smooth softening response and single crack failure mode while a double crack system is developed in the simulation with higher shear strength. Finally, it is noted that the uniaxial tensile strengths predicted in Fig. 17f are within acceptable bounds from experimental value 6.15 MPa for Standstead granite given by Mahabadi (2012).

## 4 Conclusions

Rate-dependent embedded discontinuity approach incorporating heterogeneity for numerical modeling of rock fracture was developed and extensively tested in this paper. According to the numerical simulations carried out here, the present approach captures the salient features of rock fracture in confined compression and uniaxial tension. The employed embedded discontinuity approach is particularly suitable for modeling initial microcrack population always present in natural rocks. In addition, the strain rate dependency incorporated via viscosity makes the present model capable of modeling rock fracture in dynamic conditions as well. Indeed, it was seen in the numerical simulations that the present model captures the strain rate hardening and multiple fragmentation effects involved in elevated loading rates. The model is, via the random description of material heterogeneity, also able to predict considerable variation in the uniaxial compressive strengths of numerical specimens.

It was observed in the simulations that the orientation of an introduced embedded discontinuity has a crucial effect on the nature of failure process. Namely, when an embedded microcrack (discontinuity) is parallel to the loading axis in uniaxial compression, then, as mode II opening of microcracks is severely restrained, the failure of the specimen is of stability losing nature. This results in a burst-like fragmentation of the sample as the rock columns separated by long axial macrocracks fail. This numerical failure could be interpreted as the *intragranular* parting fracture of hard rocks. In case of allowing misalignment between the plane of an embedded microcrack and the loading axis, mode II opening (sliding) develops at the embedded microcracks and, consequently, the failure process is considerably more stable having a shear band sliding nature. It is suggested here that this numerical failure corresponds to the *intergranular* shear fracture process exhibited by the majority of carbonate rocks. With this latter microcrack orientation scheme, the confining pressure-dependent brittle-to-ductile transition exhibited by compact carbonate rocks can be captured with the present approach, as was seen in the numerical simulations.

Thereby, comparing to the corresponding continuum viscoplasticity models (Rankine and Mohr–Coulomb models) the presented embedded discontinuity approach has the advantage of accounting for the orientation of the microcracks. Moreover, the present method is computationally nearly as efficient as the continuum plasticity models. Therefore, it can be considered superior to these models.

Finally, some future development topics are suggested. First, the present approach should be extended to 3D setting. Second, it would be beneficial for the reliability of the approach to formulate the underlying embedded discontinuity model in finite deformations framework. This is especially true when modeling confined compression of soft rocks since finite deformations occur in this application. Finally, grain interior plasticity related to brittle-to-ductile transition could be easily accounted for if the bulk material is described as, e.g. Mohr–Coulomb or Drucker-Prager plasticity model.

**Acknowledgments** Academy of Finland is gratefully acknowledged for funding this research through Grant no. 251626.

## References

Brancherie D, Ibrahimbegovic A (2009) Novel anisotropic continuum-discrete damage model capable of representing localized failure of massive structures: part I: theoretical formulation and numerical implementation. Eng Comput 26:100–127

Fang Z, Harrison JP (2002a) Development of a local degradation approach to the modelling of brittle fracture in heterogeneous rocks. Int J Rock Mech Min Sci 39:443–457

Fang Z, Harrison JP (2002b) Application of a local degradation approach to the analysis of brittle fracture laboratory scale rock specimens under triaxial compression. Int J Rock Mech Min Sci 39:459–476

Feist C, Hofstetter G (2006) Three-dimensional fracture simulations based on the SDA. Int J Numer Anal Met Geomech 31:189–212

Goodman RE (1989) Introduction to Rock Mechanics. Wiley, New York

Hahn GD (1991) A Modified Euler Method for dynamical analyses. Int J Numer Meth Eng 32:943–955

Huespe AE, Oliver J (2011) Crack Models with embedded discontinuities. In: Meschke G, Hofstetter G (eds) Numerical modeling of concrete cracking. CISM, Udine, pp 161–219

Huespe AE, Oliver J, Sanchez PJ, Blanco S, Sonzogni V (2006) Strong discontinuity approach in dynamic fracture simulations. Mec Comput XXV:1997–2018

Jaeger JC, Cook NGW (1971) Fundamentals of rock mechanics. Chapman and Hall, London

Jia L, Chen M, Zhang W, Xu T, Zhou Y, Hou B, Jin Y (2013) Experimental study and numerical modeling of brittle fracture of carbonate rock under uniaxial compression. Mech Res Commun 50:58–62

Klerck PA, Sellers EJ, Owen DRJ (2004) Discrete fracture in quasi-brittle materials under compressive and tensile stress states. Comput Method Appl M 193:3035–3056

Krajcinovic D (1996) Damage mechanics. North-Holland series in applied mathematics and mechanics. Elsevier, Amsterdam

Li L, Lee PKK, Tsui Y, Tham LG, Tang CA (2003) Failure Process of Granite. Int J Geomech (ASCE) 3:84–98

Liu HY, Kou SQ, Lindqvist P-A, Tang CA (2004a) Numerical studies on the failure process and associated microseismicity in rock under triaxial compression. Tectonophysics 384:149–174

Liu HY, Roquete M, Kou SQ, Lindqvist P-A (2004b) Characterization of rock heterogeneity and numerical verification. Eng geology 72:89–119

Ma G, Wang X, He L (2011) Polycrystalline model for heterogeneous rock based on smoothed particle hydrodynamics method. In: Zhao J (ed) Advances in rock dynamics and applications. CRC Press, Leiden, pp 231–251

Mahabadi OK (2012) Investigating the influence of micro-scale heterogeneity and microstructure on the failure and mechanical behaviour of geomaterials. Dissertation, University of Toronto

Mahabadi OK, Grasselli G, Munjiza A (2010) Y-GUI: A graphical user interface and pre-processor for the combined finite-discrete element code, Y2D, incorporating material heterogeneity. Comput Geosci 36:241–252

Oliver J (1996a) Modelling strong discontinuities in solid mechanics via strain softening constitutive equations. Parts 1: fundamentals. Int J Numer Meth Eng 39:3575–3600

Oliver J (1996b) Modelling strong discontinuities in solid mechanics via strain softening constitutive equations. Part 2: numerical simulation. Int J Numer Meth Eng 39:3601–3623

Pan P-Z, Feng X-T, Hudson JA (2009) Study of Failure and Scale Effects in Rocks under Uniaxial Compression using 3D Cellular Automata. Int J Rock Mech Min Sci 46:674–685

Paterson MS (1958) Experimental deformation and faulting in Wombeyan marble. Bull Geol Soc Am 69:465–476

Pininska J (2008) Models of rock deformation under uniaxial compression conditions. Geologija 50:108–115

Saksala T (2010) Damage-viscoplastic consistency model with a parabolic cap for rocks with brittle and ductile behaviour under low-velocity impact loading. Int J Numer Anal Met Geomech 34:1362–1386

Sancho JM, Planas J, Cendón DA, Reyes E, Gálvez JC (2007) An embedded crack model for finite element analysis of concrete fracture. Eng Fract Mech 74:75–86

Sellers E, Napier J (1997) A comparative investigation of micro-flaw models for the simulation of brittle fracture in rock. Comput Mech 20:164–169

Simo JC, Oliver J (1994) A new approach to the analysis and simulation of strain softening in solids. In: Bazant ZP et al (eds) Fracture and damage in quasi-brittle structures, E. and F.N. Spon, London, pp 25–39

Simo JC, Oliver J, Armero F (1993) An analysis of strong discontinuities induced by strain-softening in rate-independent inelastic solids. Comput Mech 12:277–296

Szwedzicki T (2007) A Hypothesis on Modes of Failure of Rock samples Tested in Uniaxial Compression. Rock Mech Rock Eng 40:97–104

Tang CA (1997) Numerical Simulation of Progressive Rock Failure and Associated Seismicity. Int J Rock Mech Min Sci 34:249–261

Tang CA, Hudson JA (2010) Rock Failure Mechanisms Illustrated and Explained. CRC Press, Leiden

Wang WM, Sluys LJ, De Borst R (1997) Viscoplasticity for instabilities due to strain softening and strain-rate softening. Int J Numer Meth Eng 40:3839–3864

Xia K, Nasseri MHB, Mohanty B, Lu F, Chen R, Luo SN (2008) Effects of microstructures of dynamic compression of Barre granite. Int J Rock Mech Min Sci 45:879–887

Yoon JS, Zang A, Stephansson O (2012) Simulating fracture and friction of Aue granite under confined asymmetric compressive test using clumped particle model. Int J Rock Mech Min Sci 49:68–83

Wei Y, Anand L (2008) On micro-cracking, inelastic dilatancy, and the brittle-ductile transition in compact rocks: A micro-mechanical study. Int J Solids Struct 45:2785–2798

Zhang QB and Zhao J (2014) A Review of Dynamic Experimental Techniques and Mechanical Behaviour of Rock Materials. Rock Mech Rock Eng 47:1411–1478. doi:10.1007/s00603-013-0463-y